

# Laser powder bed fusion process variation and rescanning for heterogeneous microstructural control

Anqi Liang<sup>A</sup>, Khee Siang Pey<sup>A</sup>, Tomas Polcar<sup>A</sup>, Andrew R. Hamilton<sup>A\*</sup>

<sup>A</sup> Engineering and Physical Sciences, University of Southampton, Southampton, SO17 1BJ, United Kingdom

Corresponding author: Andrew R. Hamilton. Email address: a.r.hamilton@soton.ac.uk.

## **Abstract:**

The implementation of spatially varying scanning and rescanning parameters in laser powder bed fusion (LPBF) additive manufacturing (AM) can potentially enhance the performance of metal LPBF parts by enabling controlled microstructure and property heterogeneity in a single manufacturing process. The aim of this study was to assess the variation in microstructure of 316L stainless steel (SS) by initial scanning and subsequent rescanning using different LPBF processing parameters. A range of parameters were identified by processing single laser scans to investigate the melt pool dimensions, morphology, and sub-grain cellular/dendritic microstructure. Specimens produced from the combination of multiple laser scans and multiple layers were also investigated for melt pool characteristics, sub-grain structure, and for density. Based on results, parameters were selected for fusion and densification with initial laser scanning, and different parameters were selected for subsequent rescanning and localised modifications of microstructure and properties. To better understand the link between process parameters and microstructure, the Wilson-Rosenthal equation was used to predict cooling rate ( $G \times R$ ) and correlate with sub-grain cell size. With rescanning, a refinement of the sub-grain cell size from 0.84  $\mu\text{m}$  (initial scanning region) to 0.35  $\mu\text{m}$  (rescanning region) was achieved at high density (99.96%) in 316L SS, enabling potential variations in component strength and hardness. The distribution of

microstructural refinement was dictated by the melt pool dimensions from initial scanning and rescanning relative to the powder layer height. Such variation in properties may be useful for applications requiring parts with hardened bearing surfaces, rigid mould surfaces, or localised strengthening at stress concentrations and sites of expected failure.

**Keywords:** laser powder bed fusion, Wilson-Rosenthal equation, 316L stainless steel, heterogeneous structure, sub-grain cell size, density.

## 1. Introduction

The high temperature gradients and rapid solidification rates observed in laser powder bed fusion (LPBF) additive manufacturing (AM) lead to non-equilibrium microstructures with potentially significant effects on the properties of the resulting material. In the case of 316L austenitic stainless steel (SS), LPBF processing conditions lead to the formation of cellular/dendritic sub-grain structures, associated with compositional segregation, the size of which is reported to correlate with strength according to a Hall-Petch type relationship (Wang et al., 2018). This trend of increasing strength and hardness with decreasing sub-grain cell size has been attributed to high dislocation densities at cell walls that prevent dislocation motion along continuous slip planes. Simulations suggest that oxide precipitates within cell walls may also play a role in this strengthening effect (Collins et al., 2016).

The sub-grain cell size has been reported to vary with changes in the laser power ( $P$ ) and scanning speed ( $v$ ) used in LPBF. Changes in these parameters can affect the temperature gradient at the solid-liquid interface ( $G$ ) during solidification of the melt pool, and the growth rate of the solidifying front ( $R$ ). The cooling rate of material during solidification is represented by the product  $G \times R$ , which determines the size-scale of the resulting microstructure, with finer microstructures achieved at higher cooling rates. Scipioni Bertoli et al. (2019) reported that the Wilson-Rosenthal equation, an analytical model for temperature fields around a point heat source, predicted an inverse relation between the ratio  $P/v$  and cooling rate ( $G \times R$ ), and that increasing  $G \times R$  correlated with smaller cell size and higher yield strength (from 441 to 517 MPa) in 316L SS. Wider ranges of yield strength from 325 MPa to 700 MPa have been predicted by simulations

of increased scan speed and decreased laser power due to the finer predicted microstructure and faster predicted cooling rates (Clymer et al., 2017). An increase of yield strength in LPBF 316L SS from 339.2 MPa to 519.8 MPa was reported by Wang et al. (2018) upon refinement of primary dendrite arm spacing (*PDAS*) from 0.81  $\mu\text{m}$  to 0.37  $\mu\text{m}$  due to changes in part geometry and thus suspected cooling rate. Li et al. (2020) have reported that it is dislocation density around these cells, rather than segregation cell size, that account for strengthening and so better correlates with yield strength changes. Alongside increased strength with decreased cell size, Scipioni Bertoli et al. (2019) also reported differences in porosity and corresponding decreases in ductility (from >40% to 21%), highlighting the challenge that changing process parameters to change cell size and strength can also affect densification and porosity with detrimental mechanical effects. In related work from Niendorf et al. (2014), the microstructure and properties of 316L SS were varied by varying process parameters within a build to create graded heterogeneous materials. Laser powers of 400 W (fine-grained region) and 1000 W (coarse-grained region) were employed using a specialised LPBF system with two lasers, and a corresponding decrease in yield strength from 520 MPa to 400 MPa was observed.

Correlations between porosity and LPBF processing parameters are commonly made using energy density ( $E$ ), which is a measure of the amount of energy per unit volume radiated to the powder bed at the focal point of the laser (Zhang et al., 2017). It can be calculated from  $P$ ,  $v$ , the powder layer thickness  $t$ , and the hatch spacing  $h$  between laser scans:

$$E = \frac{P}{v \times h \times t} \quad (1)$$

At low energy densities increasing  $E$  can decrease porosity, but at higher energy densities further increases tend to increase porosity. Cherry et al. (2014) reported that increasing  $E$  from 41.81 J/mm<sup>3</sup> to 104.52 J/mm<sup>3</sup> increased density of 316L SS part from 91.16% to 99.62%, and increased hardness from 162 HV to a maximum of 225 HV. However, with further increases in  $E$  up to 209.03 J/mm<sup>3</sup>, hardness dropped due to decreases in density. Porosity in excess of 5% has been reported to significantly decrease tensile strength from a maximum of 590 MPa at 97.5% relative density to 530 MPa below 95%. It has also been reported that low levels of porosity <1% do not significantly influence micro-hardness due to the high ductility of 316L SS (Yusuf et al., 2017).

Another strategy to influence microstructural features and material properties during LPBF is to implement laser rescanning, in which the laser scans the same position multiple times. The number of rescanning cycles was reported to have little effect on microstructure of LPBF Ti6Al4V, however, its ultimate tensile strength, yield strength, and micro-hardness all increased as the rescanning cycles were increased from 0 to 3 (Xiao et al., 2020). A study on the microstructure and mechanical properties of Hastelloy X superalloys after rescanning with different laser powers found that the thermal gradient and cooling rates were modified, leading to finer dendrites, a change in strain hardening rate, and an increase in ductility (Keller et al., 2020). Applying rescanning in LPBF of 316L SS showed that layer-by-layer rescanning significantly increased density to almost 100% and decreased average surface roughness ( $R_a$ ) by about 90% (Yasa and Kruth, 2011). Improved densification (from 99.23% to 99.97%) was also reported for 18Ni300 maraging steel. However, these reported benefits from rescanning come at the cost of significant increases in processing time, thus reducing

productivity and increasing cost. Localised rescanning on Ti6Al4V surface (200  $\mu\text{m}$  depth) can achieve a different grain structure and a re-orientated texture, and a modest increase in hardness by a maximum of 15% in rescan regions, while limiting added processing time and cost (Tian et al., 2018).

The aim of this study was to implement localised rescanning of 316L SS using a single-laser LPBF system, and to study the effects on relative density, sub-grain cell size, and hardness, and the spatial distribution of these changes. The effect of varying the laser power ( $P$ ) and scanning velocity ( $v$ ) for both initial scanning and for rescanning were studied. Initial scan parameters were selected for high densification, while rescanning parameters were selected for cell size refinement. To help guide the design of localised microstructural changes, results were correlated with Wilson-Rosenthal equation predictions of cooling rate ( $G \times R$ ) and melt pool dimensions. Results were also compared with single scan track experiments intended to rapidly screen for scanning and rescanning parameters that yield desired results.

## **2. Experimental procedure**

### **2.1 Laser melting experiments and sample characterization**

Gas-atomised 316L stainless steel powder (particle size normally distributed between 15  $\mu\text{m}$  to 45  $\mu\text{m}$ ) used in this study was supplied by Carpenter (USA) as CT PowderRange 316L. Prior to use, the powder mixed and sieved with reused powder and 10% fresh powder. The chemical composition specified by the manufacturer is listed in Table 1. Specimens were processed using a Concept Laser M2 LPBF 3D printer with a maximum laser power of 200 W operating in an inert argon gas environment.

Table 1 Chemical composition (wt. %) of 316L SS powders. (ADDITIVE, 2019a)

C	Fe	Cr	Ni	Mo	Mn	Si	N	O	P	S
< 0.03	Bal.	16 – 18	10 –14	2 – 3	< 2	< 1	0.1	0.1	< 0.045	< 0.03

The processing parameters in Table 2 were selected for single laser scan processing and scan tracks with a length of 10 mm were processed on a sand-blasted 316L stainless steel plate. Two tracks were scanned for each parameter. The distance between adjacent laser scans was 4 mm. A powder layer thickness of 30  $\mu\text{m}$  was used in all cases.

Table 2 Parameters for single laser scan processing.

Laser power(W)	Scanning speed(mm/s)	Linear energy density (J/mm)	Laser power(W)	Scanning speed(mm/s)	Linear energy density (J/mm)
50	50	1.00	150	150	1
	200	0.25		600	0.25
	400	0.13		800	0.19
	600	0.08		1200	0.13
	800	0.06		1600	0.09
	1600	0.03		1800	0.08
	2400	0.02		2400	0.06
	3200	0.02		3200	0.05
100	100	1	200	50	4
	400	0.25		200	1
	800	0.13		800	0.25
	1200	0.08		1600	0.13
	1600	0.06		2400	0.08
	2400	0.04		3200	0.06
	3200	0.03			

After analysing the morphology and dimensions of single laser scan melt pools and the sub-grain cell size within the melt pool, several sets of parameters were selected to manufacture uniform cubes with size of 10 x 10 x 10 mm using 5 x 5 mm island scanning strategy to investigate the microstructure and density resulting from the combination of multiple scan tracks into larger specimens. Larger multi-track specimens with an outside dimension of 23 x 20 x 10 mm were also processed with an initial set of laser scan parameters, (termed “A”, selected for high densification)

followed by various rescanning parameters (termed “B<sub>1</sub>”, ..., “B<sub>n</sub>”), selected to modify the sub-grain cell size. Rescanning process was carried out by first scanning a layer with the initial parameter A, and then rescanning the layer with parameter B following the same direction as initial scans. Scanning was rotated by 90 degrees between each layer. In order to study the effect of rescanning on microstructural heterogeneity, 1, 5, 10, and 20 layers of rescanned layers were processed in a single component, each separated by a constant spacing of 20-layers scanned with initial A parameters (Fig. 1). A stepped edge was used to identify each rescan region.

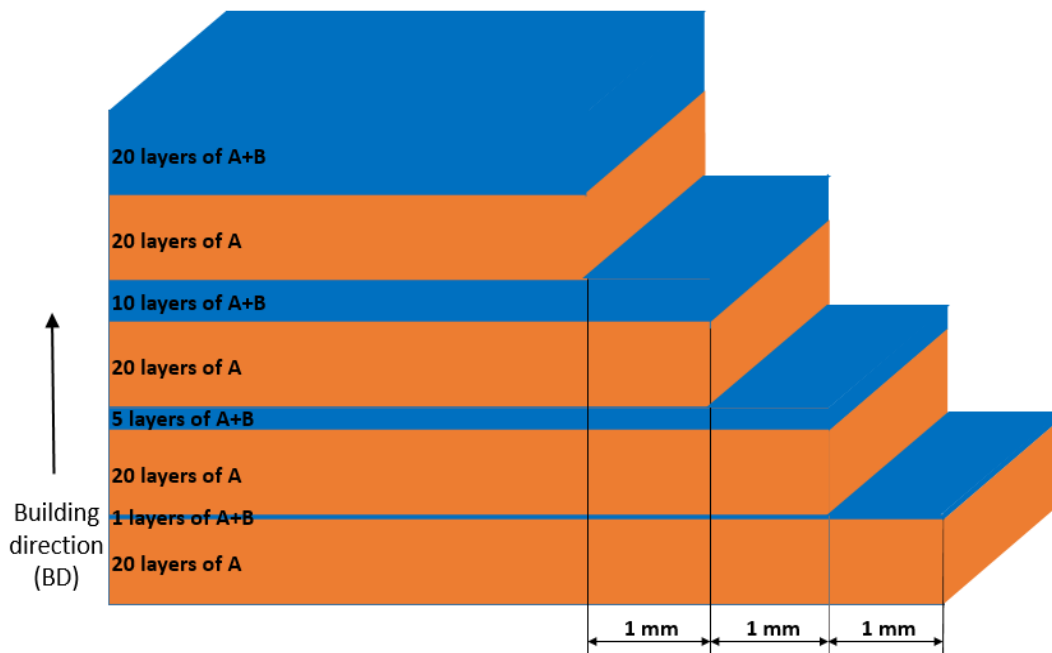


Figure 1 Cross sections of components containing 1, 5, 10 and 20 layers of rescanning. Orange represents tracks scanned uniformly by initial A parameter, blue represents the tracks scanned first by parameters A, and then rescanned by parameters B.

The dimensions of the melt pools (defined in Fig. 2) were measured using an Olympus BX41M-LED optical microscopy (OM) (Tokyo, Japan). For single laser scans, the average width of melt pools was measured from the top view at three positions for each track, and depth was measured from the cross-sectioned plane near the middle of each track. The height and surface profiles of single tracks were measured with an Alicona G4 InfiniteFocus using variable focus measurement capability. The sub-grain



cellular structure within melt pools was observed using a Carl Zeiss Leo 1450VP scanning electron microscopy (SEM) with Oxford Instruments Energy Dispersive Spectrometer. The cell size was measured by the line method according to ISO (2017), with averages and standard deviations calculated from 25 measurements at 5 random positions on each surface. Before cross-sectional observation, samples were cut by Mecatome T210 precision automatic micro-cutting machine, mounted in KonductoMet<sup>®</sup> Resin, which is a conductive thermosetting phenolic compound, ground using 120, 800, 1200, and 4000 grits abrasive paper, and polished using 1  $\mu\text{m}$  diamond paste to obtain mirror-like surface finish. To reveal the microstructures, the polished surface was etched by Kalling's No.2 reagent (50 mL HCl, 50 mL ethanol, 2 g copper chloride) for approximately 10 s.

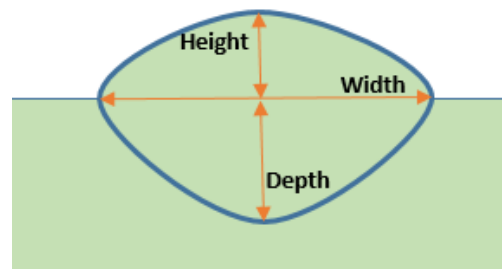


Figure 2 Schematic of single melt pool shape and dimensions, from side view.

The overall porosity of specimens was measured by Archimedes' method according to ASTM (2017). Measurement of each sample was repeated five times to obtain averages and standard deviations. Local porosity in different initial or rescan regions was examined using OM after grinding and polishing, but before etching. Digital images were captured by OM and converted into a binary, black and white image. Threshold values were selected manually to enable identification of pores, and porosity was calculated as an area volume fraction of black to white pixels. The hardness measurement of the rescanned specimen in both initial scanning and

rescanned regions was carried out by a Nanotest Vantage nanoindenter (Micro Materials Ltd) applied with a Berkovich tip and indenter tip shape factor was taken into account in the analysis. Tests were performed in accordance with ASTM (2015) in a load-controlled mode, the maximum indentation load was set to 60 mN and spacing between adjacent indentations were 40  $\mu\text{m}$ . Averages and standard deviations were calculated from at least 10 measurements along a straight line in initial scanned region and 20-layer rescanned region. In the rescanned region, only indents within rescanned melt pools were included in the average.

## **2.2 Model for calculation of solidification parameters**

The Wilson-Rosenthal equation is an analytical model of heat transfer from a point-source to a semi-infinite planar work piece. The attractiveness of this model lies in its simplicity and low computational cost for very large numbers of points compared to fully numerical techniques. However, the model cannot consider complex boundary conditions and it assumes steady state conditions meaning that it cannot be used to predict the effects of complex beam paths. Furthermore, the thermal properties (thermal conductivity, specific heat capacity) are assumed temperature-independent, with the values taken at the melting point (Table 3), the latent heat of solidification is neglected. The surface of the work piece is considered insulated (no radiative heat transfer) and convection within the melt pool at the heat source is neglected. In the past, this model has been applied to welding processes (Rosenthal, 1941). Its application to LPBF processes additionally neglects the effects of unfused metal powder at the surface of the work piece (Ye et al., 2018).

Table 3 Thermal properties for 316L SS used in Wilson-Rosenthal equation.

Property	Value	Unit	Reference
Room Temperature, $T_0$	25	°C	
Melting Point, $T_M$	1385	°C	(Mills, 2002)
Thermal Conductivity, $k$	12.45	W/mK	(Additive, 2019b)
Specific heat, $c_p$	468	J/kgK	(Additive, 2019b)
Thermal Diffusivity, $\alpha$	$3.4 \times 10^{-6}$	m <sup>2</sup> /s	(Additive, 2019b)
Absorptivity, $\varepsilon$	0.58		(Rubenchik et al., 2015)

Despite the simplifying assumptions described above, the Wilson-Rosenthal equation has been used to predict accurate solidification parameters which are in good agreement with experimental data (Scipioni Bertoli et al., 2019). It predicts the three-dimensional, steady-state temperature field for a point heat source moving in the x-direction as follows (Equation 2) (Promoppatum et al., 2017):

$$T = T_0 + \frac{P\varepsilon}{2\pi k\sqrt{x^2 + y^2 + z^2}} \exp\left[-\frac{v}{2\alpha}\left(x + \sqrt{x^2 + y^2 + z^2}\right)\right] \quad (2)$$

where  $T_0$  is the initial temperature,  $P$  is the laser power,  $\varepsilon$  is the laser absorptivity, taken here as 0.58, as suggested for 316L SS (Rubenchik et al., 2015).  $k$  is thermal conductivity,  $v$  is the scanning speed,  $\alpha$  is the thermal diffusivity, and  $\sqrt{x^2 + y^2 + z^2}$  is the distance from beam location to the point of interest.

The temperature fields were calculated using Equation 2 in MATLAB®. The size of plot domain was selected such that it contains the entire melt pool and remains consistent for a different set of processing parameters to identify the melt pool boundaries clearly. The size of calculation domain was determined by  $i$  (number of adjacent scan tracks taken into consideration),  $L$  (track length), and *plot domain sizes in x-, y-, and z-directions*. X-direction calculation domain size must be greater than  $(2 \times iL + \text{plot domain size in x direction})$ . Y-direction calculation domain size must be at least  $((i - 1) \times \text{hatch spacing} + i \times \text{plot domain size in x direction})$ . Z-direction calculation domain size must be at least equal to plot domain size in z direction. Temperature

was calculated at points with spacing of 0.5  $\mu\text{m}$  in depth, 2.5  $\mu\text{m}$  in width and 5  $\mu\text{m}$  in length. Substrate temperature was assumed constant at 25  $^{\circ}\text{C}$ . To simulate the temperature distribution of a single track with varying parameters, the solution was iterated for different combinations of laser power and scan speed (Table 2). Superposition of the temperature fields for the heat source at different locations and times was used to model the temperature field in multi-track and rescanned specimens.

### **3. Results and discussions**

#### **3.1 Single-scan experiments**

The melt pools from single laser scans processed as specified in Table 2 were classified into three representative morphologies: keyhole tracks (Figure 3 (a)), conduction mode (Figure 3 (b)), and discontinuous tracks (Figure 3 (c)), according to depth-to-width aspect ratio ( $DWR$ ). Eagar and Tsai (1983) reported that the cross section of a melt pool formed in conduction mode is approximately semi-circular so that  $DWR \cong 0.5$ . King et al. (2014) proposed that keyhole melting, caused by excessive energy penetration, can be identified by  $DWR > 0.5$ . Severe keyhole mode can cause porosity defects due to turbulent gas entrapment and melt pool vaporization (Saunders, 2017). Discontinuous tracks due to insufficient heat show a large variation in height along the scan track and sometimes drop below the base plate under the powder layer, which may cause the incomplete fusion and bonding between adjacent tracks and layers, and therefore induce porosity defects.

The dimensions (width and depth) of melt pools from single laser scans and the variation of melt pool dimension with energy density are shown in Figure 4. Linear energy density, defined as  $P/v$ , can be used to quantify energy per unit length for single

laser scans, rather than energy per unit volume since hatch spacing is not defined and layer thickness is constant. For each laser power except 50 W, the width and depth of melt pools increased with increasing energy density due to larger input energy, which is consistent with other reports (Matilainen et al., 2014). Melt pools processed with a laser power of 50 W deviated from this trend in width because low laser power was more likely to form discontinuous tracks due to insufficient energy density.

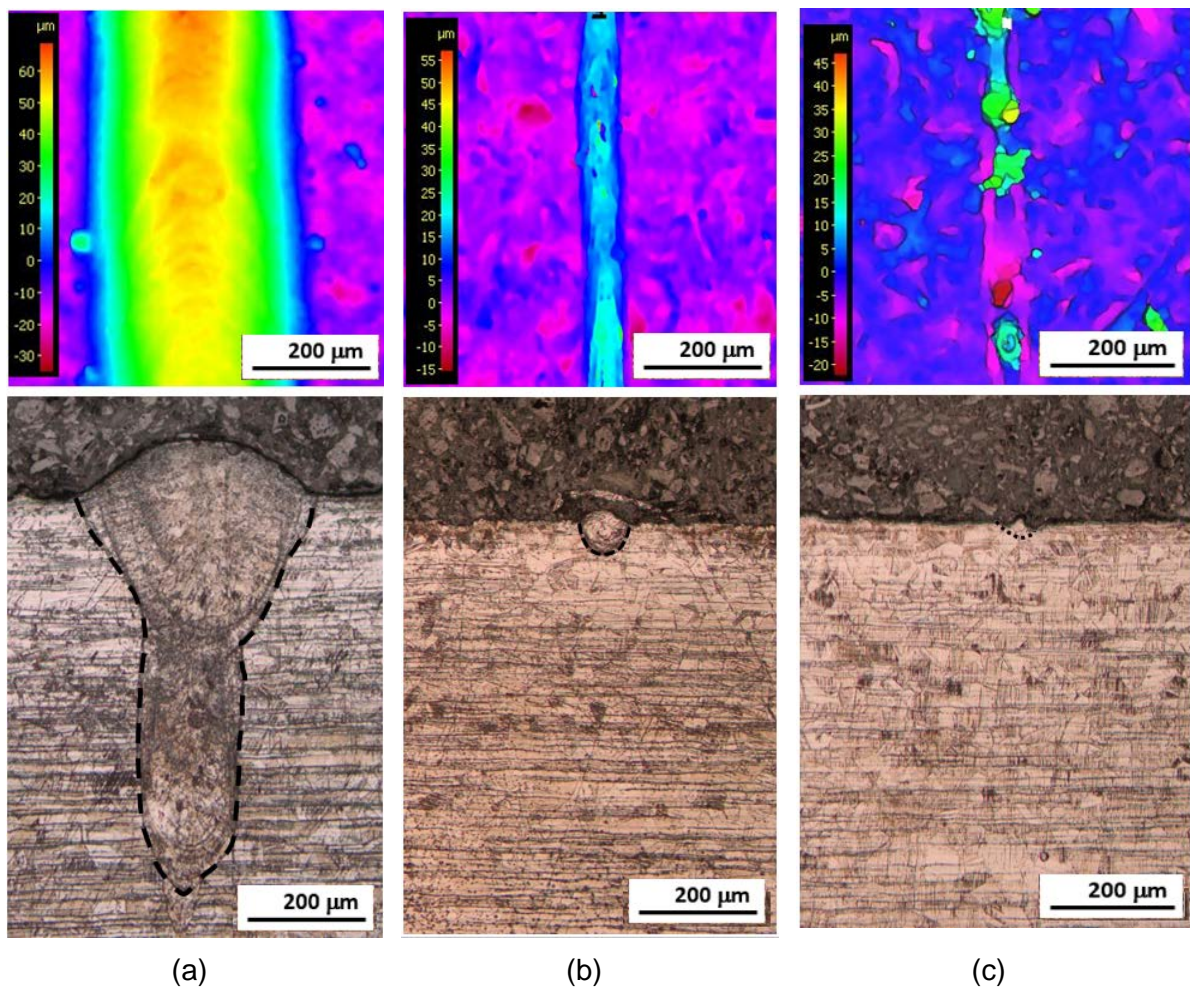


Figure 3 Top views of height profiles (top row) and side views of cross-sectioned melt pools (bottom row) representative of (a) continuous melt pool in keyhole mode; (b) continuous melt pool in conduction mode; (c) discontinuous melt pool. The boundary of the melt pools are indicated with black dash lines.

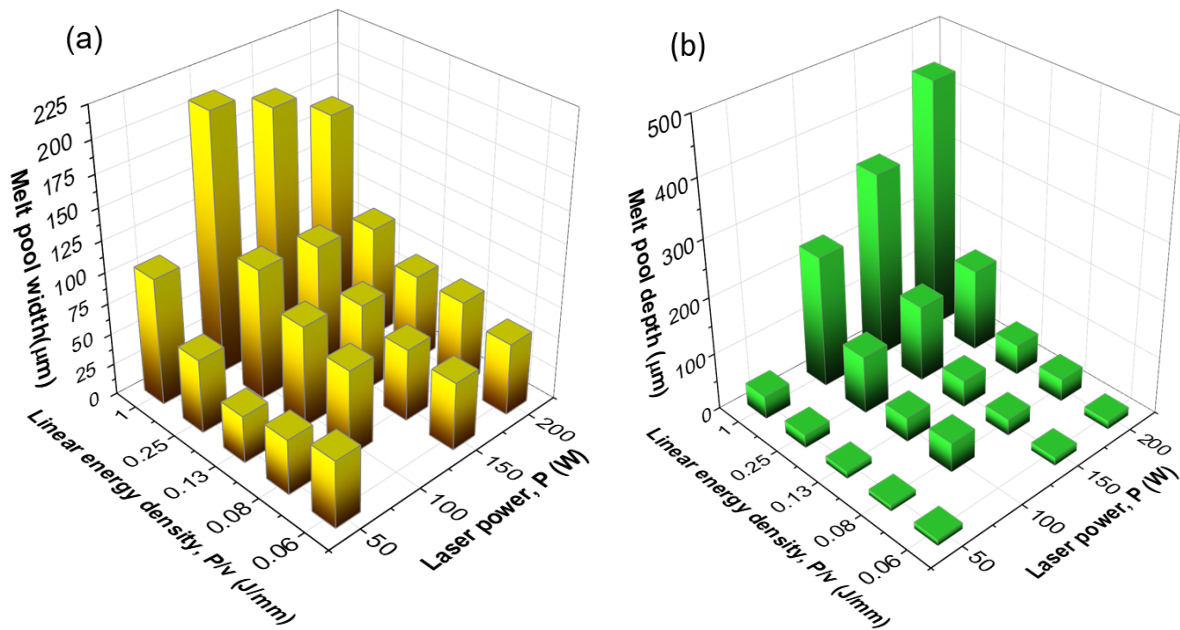


Figure 4 (a) Average width and (b) depth of single laser scan tracks with different linear energy densities and laser powers. The experimental scatter was up to 21.93% of widths and 27.86% of depths.

A sub-grain dendritic/cellular structure was observed within the melt pools, as shown in Figure 5. In Fig. 5 (a), grains (outlined in blue) are radially oriented within the melt pool and elongated in the direction of solidification, which is perpendicular to the melt pool boundaries, as reported by Casati et al. (2016). Fig. 5 (b) shows that each grain contains a colony of sub-grain cellular dendrites oriented in the same direction as the grains. By varying LPBF process parameters, the cell size changed due to variation in solidification rate caused by different linear energy density, as shown in Figure 6. With a constant laser power, cell size increased with increasing  $P/v$  values (due to decreasing scan speed), which can be attributed to lower cooling rate within melt pools (Clymer et al., 2017).

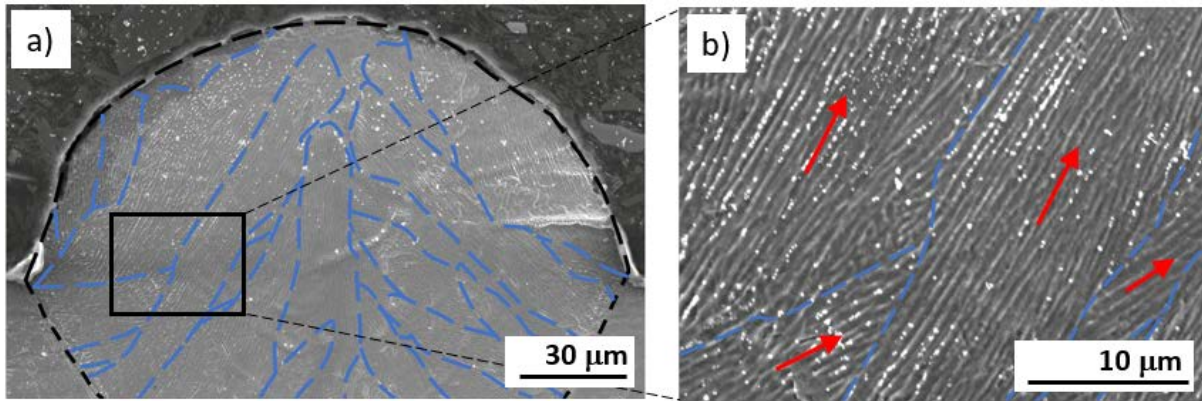


Figure 5 SEM images of single laser scan tracks showing (a) grains and (b) sub-grain cellular dendrite structure. The melt pool boundary is marked by a black dash line, blue dash lines mark grain boundaries, and red arrows indicate the growth direction of cellular dendrites.

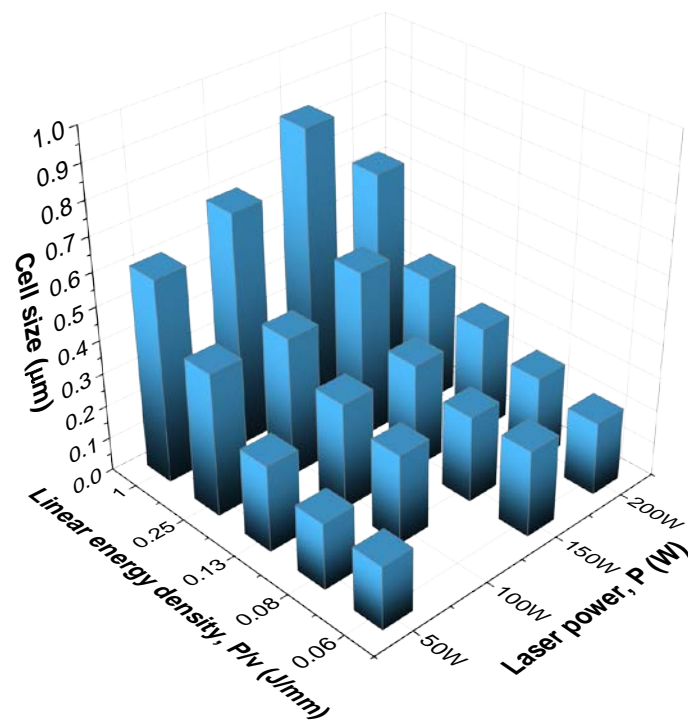


Figure 6 Cell size of single laser scan tracks with different linear energy density and laser power. Experimental scatter was up to 26.92%.

A P-v plot (Figure 7) summarizes the morphology and sub-grain cell size of single scan tracks. Both cell size and  $DWR$  were higher in regions where linear energy density ( $P/v$ ) is higher, indicating that with increased energy, melt pools became deeper and sub-grain cellular structure became coarser due to a slower cooling rate, while lower  $P/v$  resulted in discontinuous tracks due to insufficient energy input, which is consistent with literature from Guo et al. (2018). The regions of continuous tracks with  $DWR < 1$

are likely to achieve LPBF components with a high level of density. In these regions (yellow and blue), the largest and smallest average cell sizes measured were  $0.85\ \mu\text{m}$  and  $0.26\ \mu\text{m}$ , respectively.

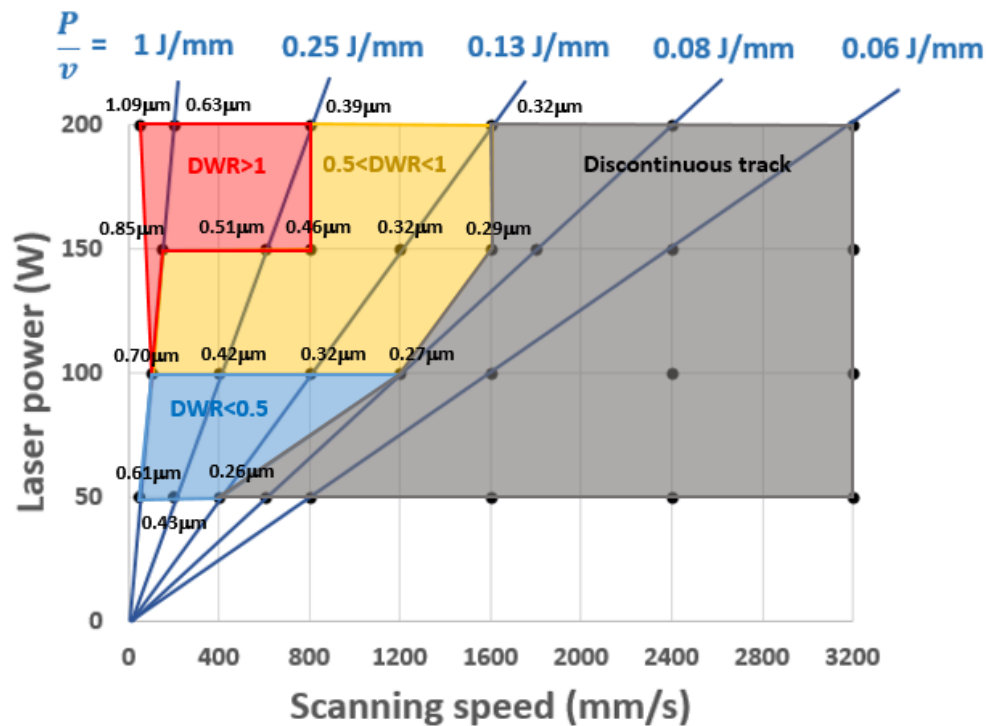


Figure 7 Laser power-scan speed,  $P$ - $v$ , plot summarising morphology and sub-grain cell size of tracks with varying processing parameters. Regions of severe keyhole tracks ( $DWR > 1$ ), slight keyhole tracks ( $0.5 < DWR < 1$ ), and discontinuous tracks are marked in red, yellow, and gray shading, respectively. Average cell size is specified above each data point.

### 3.2 Single-scan simulation

After the temperature field was obtained from Wilson-Rosenthal equation, the melt pool boundary of single-scan melt pool was obtained as the locations where the temperature was predicted to drop below the melting point. The predicted melt pool depth (black points) as a function of linear energy density is shown in Figure 8 and compared with measured depth from experiments at 200 W, 150 W, 100 W, and 50 W (blue, orange, grey, and yellow rectangular points). Although the predicted trend of increasing depth with increasing  $P/v$  matched experimental results, predictions for individual sets of processing parameters were not accurate in most cases due to the assumptions of this modelling, which results in predicted melt pool shape with constant



$DWR=0.5$ . Only a minority of melt pools in conduction mode were experimentally observed to have a shape with  $DWR$  of 0.5. At lower linear energy densities, the measured depth was smaller than the predicted depth because of the shallow melt pool and discontinuous tracks; conversely, at higher linear energy density, the experimental results were larger than the predicted depth due to keyhole mode.

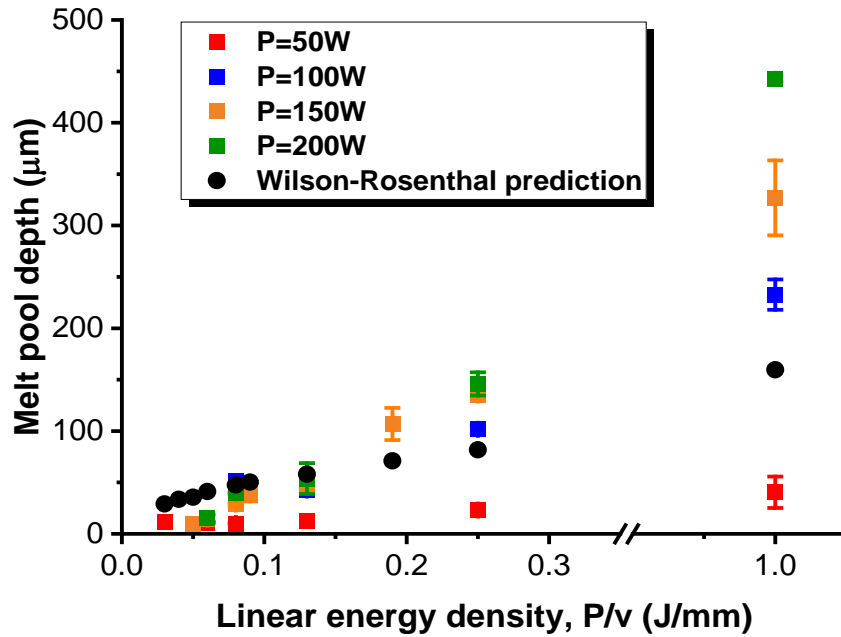


Figure 8 Predicted and measured depths of melt pools from single laser scans as a function of the linear energy density,  $P/v$ .

The predicted cooling rate  $G \times R$  from the 29 sets of parameters is plotted in Figure 9 with respect to linear energy density ( $P/v$ ), which was found to be inversely proportional to the  $P/v$ , as expected. The data were fitted using a power law, yielding the relationship between linear energy input and cooling rate in Equation 3:

$$G \times R = 1.6 \times 10^5 \left(\frac{P}{v}\right)^{-1.182} \quad (3)$$

The exponent of the fitted power law indicates that cooling rate close to linear proportionality with the inverse linear energy density,  $v/P$ . Similar predictions obtained by Scipioni Bertoli et al. (2019) are also shown in Figure 9. Slight deviation between these curves can be explained by the different absorptivity values, 0.58 for this study

and 0.35 for the others. In addition, an analytical expression obtained from Wilson-Rosenthal's equation for the cooling rate of a point along the laser travelling direction provided by Kistler et al. (2017) also gave an inverse relationship with linear energy density (Equation 4):

$$\frac{dT}{dt} = 2\pi k \frac{v}{P} (T_m - T_0)^2 \quad (4)$$

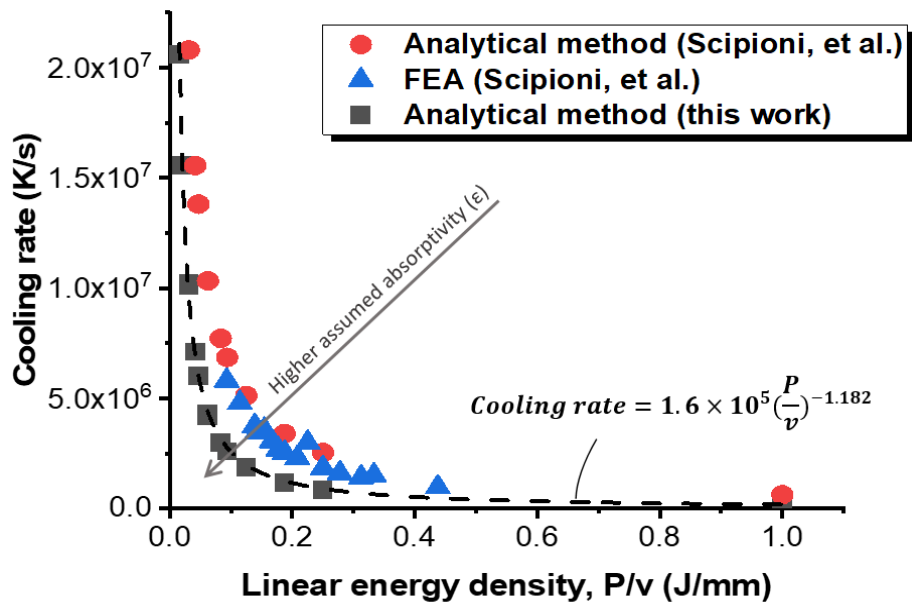


Figure 9 Cooling rate,  $G \times R$ , expressed as a function of the linear energy density,  $P/v$ .

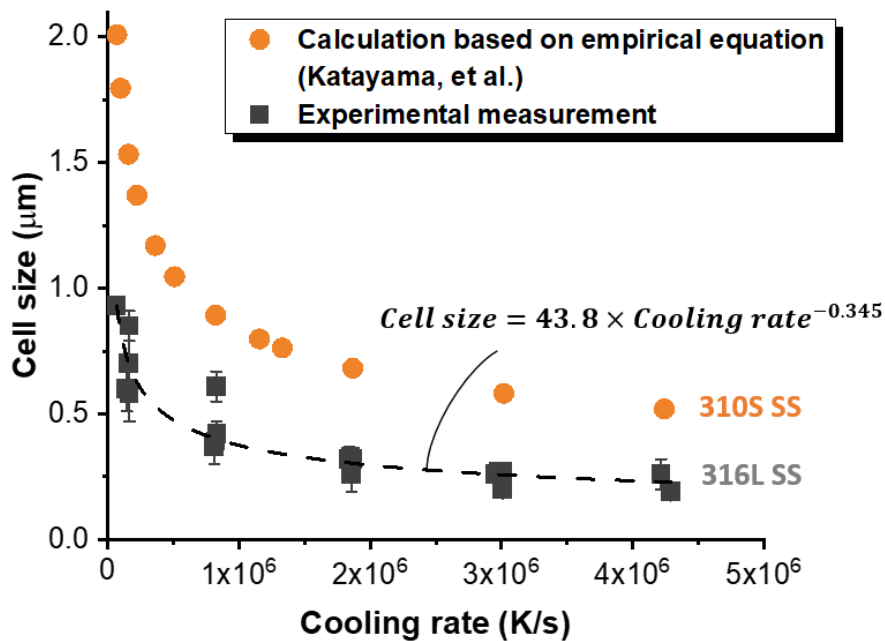


Figure 10 The experimentally measured cell size obtained with CL M2 printer and calculated cell size based on empirical equations are shown as a function of predicted cooling rate.

A study by Katayama and Matsunawa (1984) correlated cell size ( $d$ ) with cooling rate ( $G \times R$ ) for austenitic stainless steels, with an equation (Equation 5) in the general form:

$$d = A \cdot (G \times R)^n \quad (5)$$

where  $A$  and  $n$  are constants related to the materials. Also, in their study, an empirical equation was obtained for 310S SS (Equation 6):

$$d = 80 \cdot (G \times R)^{-0.33} \quad (6)$$

Both 316L SS and 310S SS are austenitic stainless steels, however, the solidification processes and ferrite contents differ. The measured cell sizes of 316L SS (black points) from single-scan experiments at corresponding predicted cooling rates are shown in Figure 10 and compared with values from the empirical equation of 310S SS (orange points). The predicted trends are similar, with a near-constant shift in predicted values that can be attributed to the different compositions of SS. Therefore, the power law fit for measured cell size as a function of cooling rate for 316L SS from is given as Equation 7:

$$d = 43.8 \times (G \times R)^{-0.345} \quad (7)$$

Combining Equation 3 and 7, a direct relationship between linear energy density and cell size was obtained as Equation 8:

$$d = 0.7 \times \left(\frac{P}{v}\right)^{0.41} \quad (8)$$

### 3.3 Multi-layer part fabrication

From the results of single laser scan experiments, five sets of parameters were chosen and listed in Table 4 in descending order of cell size (from 0.85  $\mu\text{m}$  to 0.26  $\mu\text{m}$ ) measured in single laser scans. To enable manufacture of parts with a large difference in cell size, and therefore large expected differences in hardness and strength, two parameters corresponding to maximum (A1, A2) and one for minimum cell size (A5) were selected from the boundaries between severe keyhole region and slight keyhole

region, and the boundaries between continuous and discontinuous regions as shown in Figure 7. Two parameters in region of  $DWR < 1$  with intermediate cell sizes were also chosen (A3, A4). In order to avoid lack of fusion defects between adjacent scans, the hatch spacings in Table 4 were chosen as 70% of the expected track width based on single scan tracks (resulting in 30% overlap between adjacent scans) (Di et al., 2011).

Table 4 Processing parameters used for multi-layer specimen manufacture.

Parameter number	A1	A2	A3	A4	A5
Cell size from single scans ( $\mu\text{m}$ )	0.845	0.700	0.320	0.316	0.258
Laser power, $P$ (W)	150	100	150	100	50
Scan speed, $v$ (mm/s)	150	100	1200	800	400
Hatch spacing, $h$ ( $\mu\text{m}$ )	133.5	145.3	50.8	57.1	26.5
Energy density, $E$ ( $\text{J}/\text{mm}^3$ )	249.69	229.41	82.02	72.97	157.23
Linear energy density, $P/v$ ( $\text{J}/\text{mm}$ )	1	1	0.13	0.13	0.13

The density of multi-layer cubes was measured by both Archimedes method and OM and are compared in Figure 11. A target density level of 99% for little or no impact on quasi-static mechanical properties (Yusuf et al., 2017) is indicated by a red dashed line. The density measured from OM was 1.59% – 3.99% higher than the density from Archimedes method, but the Archimedes method was considered more reliable as the whole sample volume was taken into account instead of discrete cross sections, which may not represent an overall porosity of the sample. Furthermore, the standard deviation of the Archimedes method ( $< 0.35\%$ ) is lower than for OM ( $< 1.41\%$ ), especially for parts with lower densities. The higher density determined by OM might be attributable to pores with a size smaller than or close to the resolution of the microscope, which may not be captured by the thresholding procedure used in the image analysis of density. Comparing the density of cubes measured by OM method,

cubes processed with parameters A1 and A2 (with highest energy densities of 249.69 J/mm<sup>3</sup> and 229.41 J/mm<sup>3</sup>) showed highest densities of 99.6% and 99.9%, while cubes with parameters A3 and A4 (processed with lowest energy densities of 82.02 J/mm<sup>3</sup> and 72.97 J/mm<sup>3</sup>) had lower densities of 97.0% and 96.4%. Despite a higher energy density than cubes A3 and A4, cube A5 (157.23 J/mm<sup>3</sup>) exhibited the lowest density of 91.2%, possible reasons for which are discussed below.

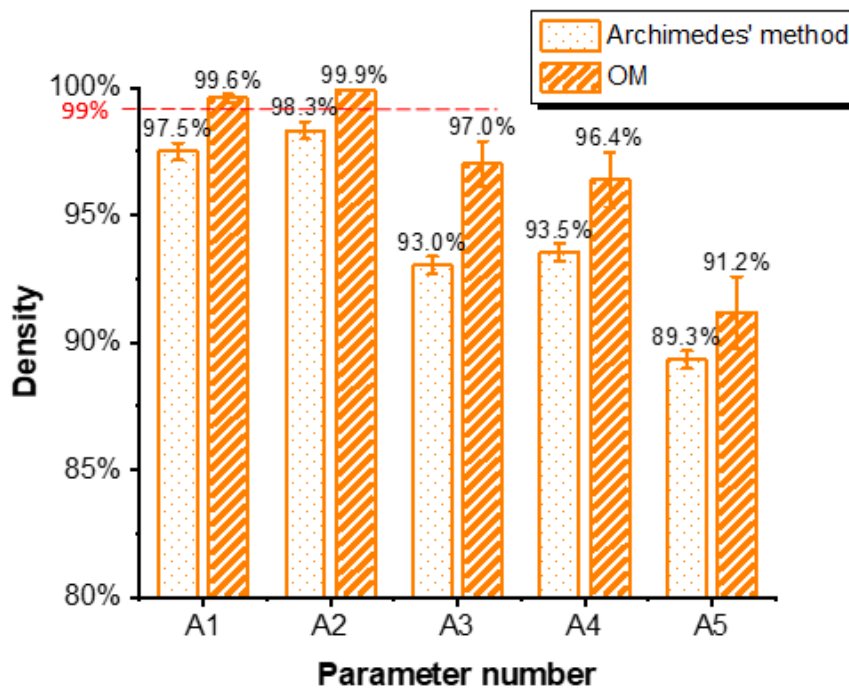

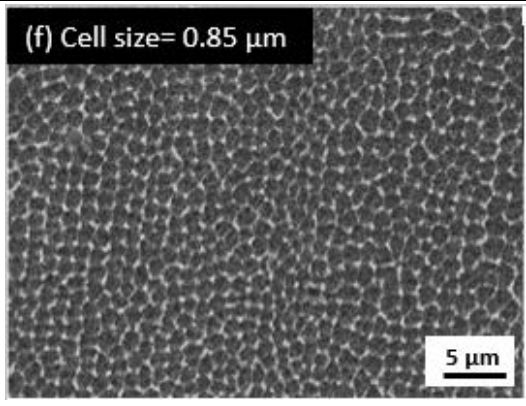
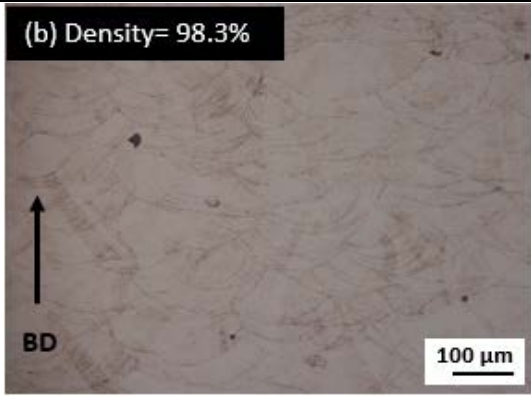
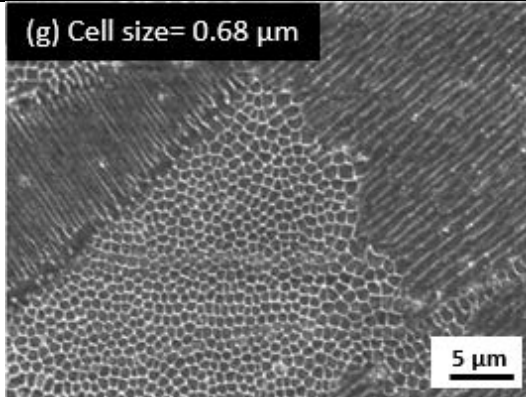


Figure 11 Density of five cubes produced via different processing parameters measured by both Archimedes method and optical microscopy. Error bars bound one standard deviation.

The shapes and distribution of pores within multi-layer specimens processed with each different parameter are displayed in Fig. 12 (a) – Fig. 12 (e). As shown in Fig. 12 (a) and (b), pores in cubes A1 and A2 (with highest energy densities of 249.69 J/mm<sup>3</sup> and 229.41 J/mm<sup>3</sup>) were mostly spherical in shape and small in size, and mostly distributed within melt pools. This suggests the pores were gas-induced by high laser energy, turbulent melt pool dynamics, vaporization of low melting point constituents (Zhang et al., 2017) or gas-induced voids embedded within the powder feedstock (Hao et al., 2009). However, cubes A3, A4, and A5 (with lower energy densities than cubes A1

and A2) showed irregular, non-spherical and larger pores, suggesting process-induced porosity formed by insufficient melting or lack of fusion between adjacent scan tracks and/or successive layers (King et al., 2014). The pores in cube A3, A4, and A5 (Fig. 12(c–e)) were mainly located beneath the boundaries of the melt pools and some un-melted powders were observed adjacent to a triangular void, which suggests lack of fusion due to insufficient energy density input. Although cube A5 had a higher energy density ( $157.23 \text{ J/mm}^3$ ) than cubes A3 and A4 ( $82.02 \text{ J/mm}^3$  and  $72.97 \text{ J/mm}^3$ ), ~4% lower density was exhibited. This can be explained by the discontinuity of single laser scans produced using the A5 parameters, and a melt pool size (height plus depth of  $29.2 \text{ }\mu\text{m}$ ) slightly smaller than the powder layer thickness of  $30 \text{ }\mu\text{m}$ .

Parameter No.	Pores shape	Sub-grain structure
A1	<p>(a) Density= 97.5%</p> 	<p>(f) Cell size= 0.85 μm</p> 
A2	<p>(b) Density= 98.3%</p> 	<p>(g) Cell size= 0.68 μm</p> 

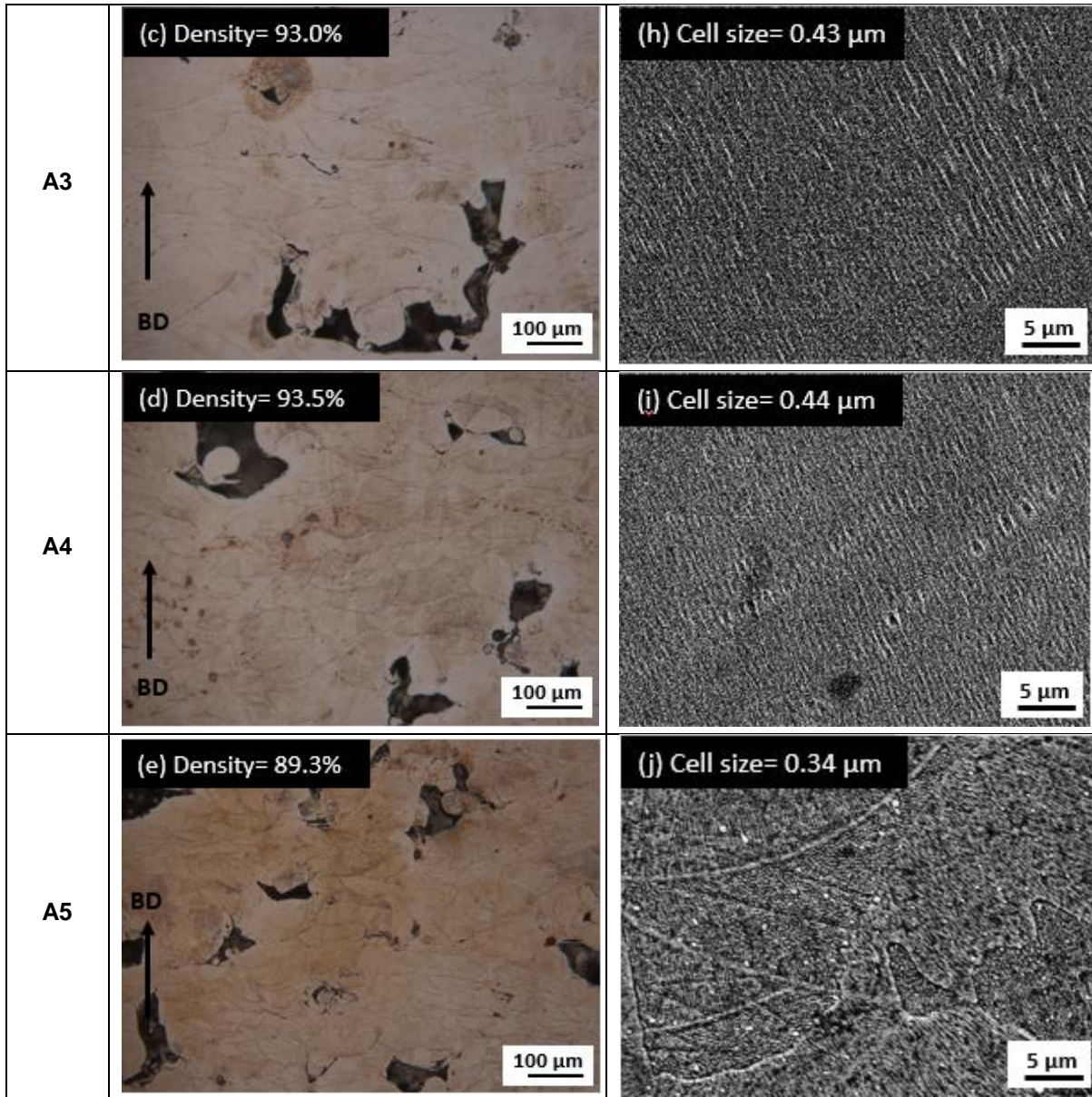


Figure 12 Pore morphology and sub-grain structure for five cubes processed using parameter A1–A5, as indicated.

The sub-grain cellular structures of multi-layer specimens are shown in Fig. 12 (f–j), and the average cell size is given on each corresponding image. Building direction (BD) is also indicated. With decreasing  $P/v$  from 1 to 0.13 J/mm, the cell size decreased from ranges of 0.68–0.85 μm to 0.34–0.45 μm. These average values with standard deviations (orange points) are shown in Figure 13, together with predicted cell size of multi-layer tracks from the Wilson-Rosenthal equation (grey points) and measured cell size from single scan track experiments (black points). The cell size

measured in multi-layer cubic specimens and single tracks are not significantly different (P-value of 0.71 from unpaired T-tests, indicating a low probability of difference), and the Wilson-Rosenthal model predictions again showed good agreement with experimental measurements of cell size in both single tracks and multi-layer cubes.

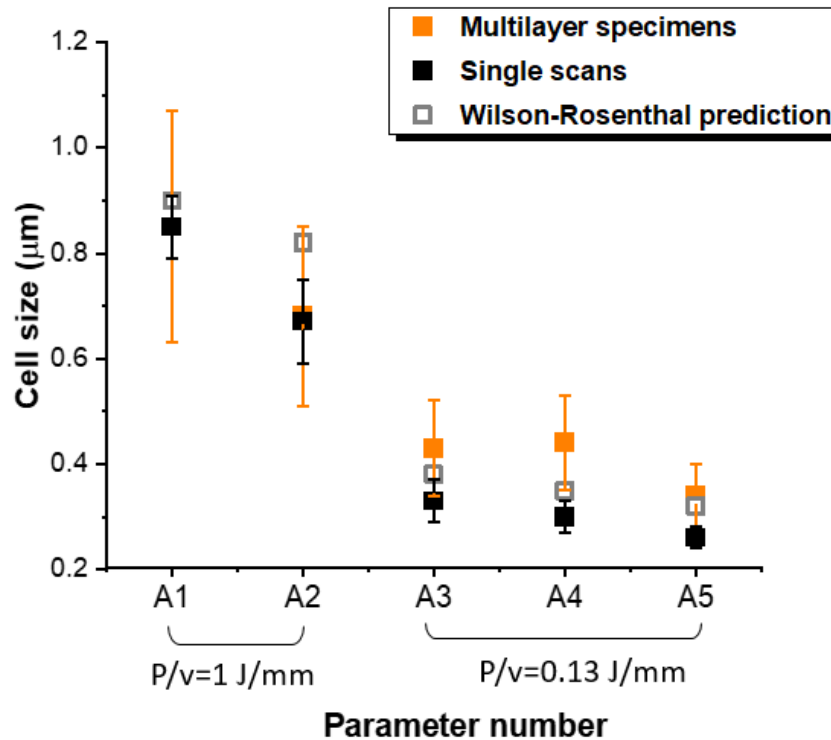


Figure 13 Cell size for five cubes processed using parameter A1–A5, as indicated.

### 3.4 Multi-layer fabrication with rescanning

Without rescanning, little variation in cell size (0.68–0.85 µm) was achieved while maintaining high densities (>97.5%) for multi-layer parts (i.e. cubes processed with parameters A1 and A2, Table 4 and Fig. 11, 12). Therefore, initial scanning was implemented to achieve high densification, with rescanning using different laser parameters to achieve a larger variation in cell size. The parameter A1 was selected as the initial parameter (Parameter A) for high densification (> 97.5%) and a coarse cell size of 0.85 µm. Rescanning parameters (B<sub>n</sub> parameters) with finer cell sizes were



selected to achieve large differences in cell size in initial and rescan regions. Based on results from the P-v plot in Figure 7, rescanning parameters were selected from the boundaries between continuous tracks and discontinuous tracks for small cell size, as listed in Table 5 (Note: B1 parameters are the same as parameter A5 in Table 4).

Table 5 Parameters for rescanning experiment.

	A	B1	B2	B3	B4
Cell size from single scans ( $\mu\text{m}$ )	0.845	0.258	0.323	0.291	0.273
Laser power, $P$ (W)	150	50	200	150	100
Scan speed, $v$ (mm/s)	150	400	1600	1600	1200
Hatch spacing, $h$ ( $\mu\text{m}$ )	133.5	42.8	80	39.6	53.3
Energy density, $E$ ( $\text{J}/\text{mm}^3$ )	249.69	97.35	52.08	78.91	52.12
Linear energy density, $P/v$ ( $\text{J}/\text{mm}$ )	1.00	0.13	0.13	0.09	0.08

Melt pools in different regions with either 1, 5, 10 or 20 layers of rescanning (specimen detailed in Fig. 1) are shown in Figure 14 for A+B4 initial+rescan parameters. Rescanned melt pools were identified by the difference in contrast after etching, as confirmed by the refined cell size measured from SEM images. For 1-layer of rescanning (Fig. 14(a)), the rescanned melt pools (marked in blue lines) were mostly covered by the next layer of initial scanning melt pools (shown in orange lines) so that the proportion of refined microstructure within the layer from rescanning was small. With increasing layers of rescanning, as shown in Fig.14 (c) and (d), the proportion of rescanned melt pools within layers appeared to increase and were arranged more continuously along layers. This might be explained by the expected effect of rescanning on surface quality and reduced roughness ( $R_a$  decreases from  $12 \mu\text{m}$  down to  $1.5 \mu\text{m}$  have been reported by Yasa and Kruth (2011)).

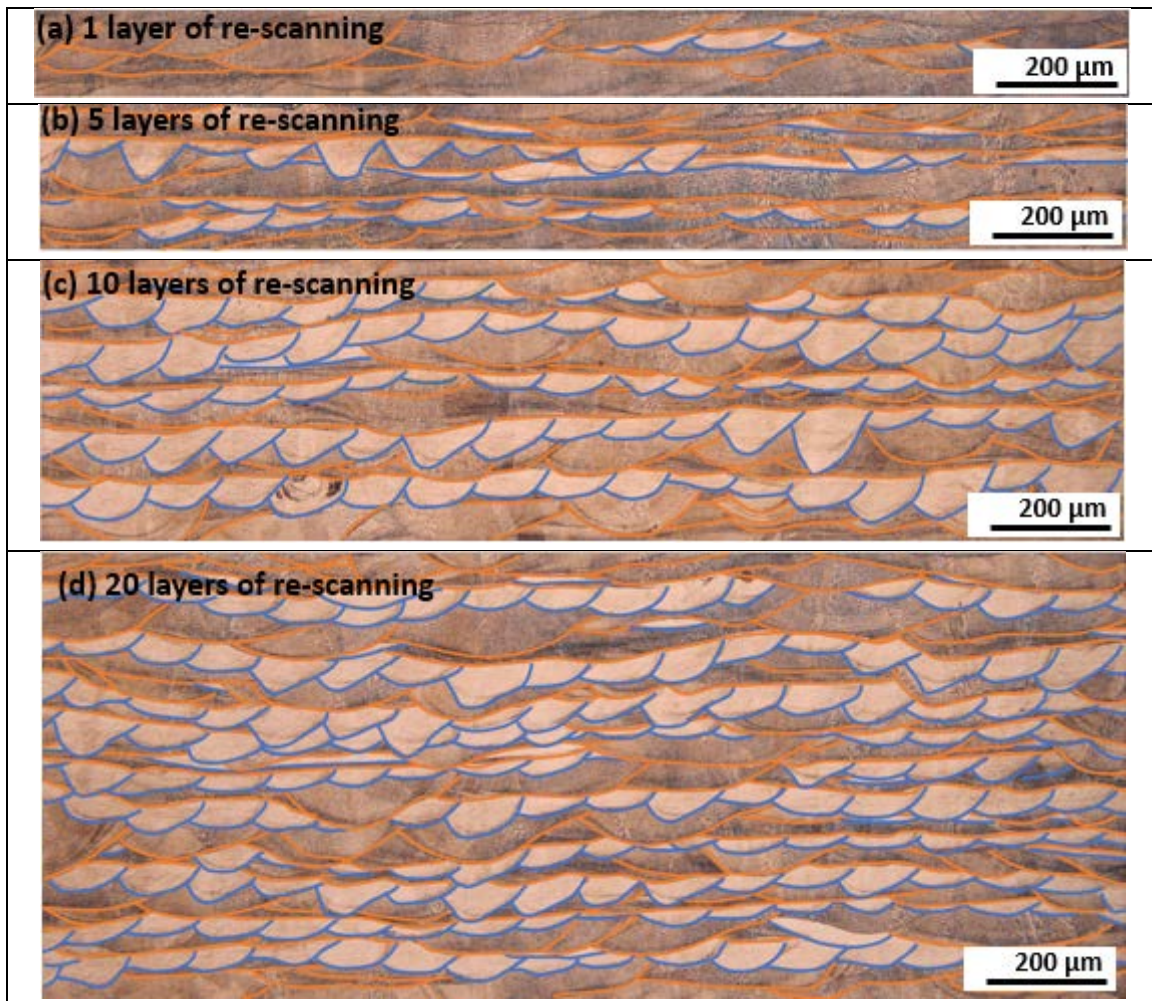


Figure 14 Comparison of melt pool distribution after 1, 5, 10, and 20 layers with rescanning using parameters A+B4. Blue lines indicate rescanning melt pool boundaries from parameter B4 and orange lines represent melt pool boundaries of initial scanning with parameter A.

The sub-grain microstructure in initial and rescanned regions were investigated in regions with 20 layers of rescanning for each combination of A and B<sub>n</sub>. As shown in Figure 15, the local densities of regions with 20 layers of rescanning (A+B1, A+B2, A+B3, and A+B4) were measured by OM and compared with the density (also measured by OM) of the uniform specimen processed with initial parameter A (Parameter A1 from Figure 11). All rescanning regions had densities 0.27–0.41% higher than the specimen processed with initial parameter A only. This effect was observed for laser parameters that resulted in high porosity and lack of fusion as initial scan parameters (A5,  $P = 200$  W,  $v = 400$  mm/s) when they were used as rescanning

parameters ( $B1$ ,  $P = 200$  W,  $v = 400$  mm/s). Similar results were also reported by Yasa et al. (2011) who found porosity reduced from 0.77% to 0.036% with rescanning.

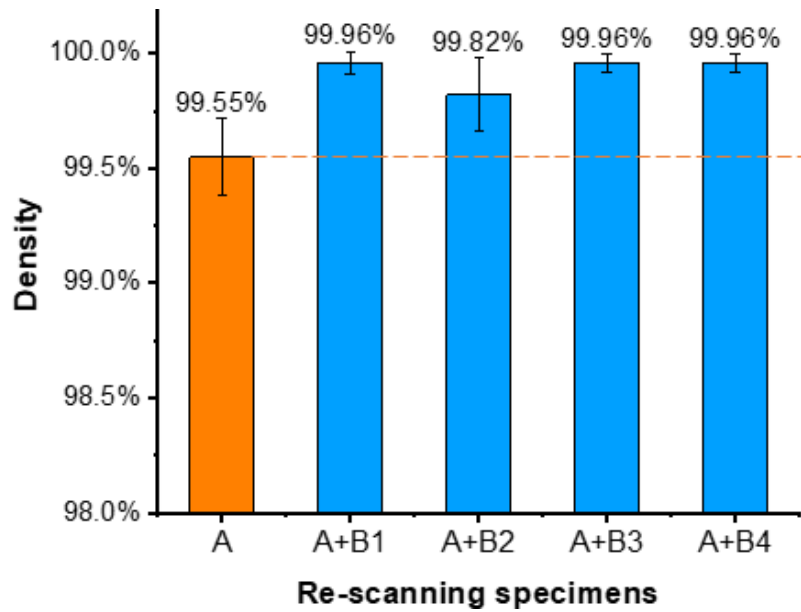


Figure 15 Optical micrograph measurements of local density at regions with 20 layers of rescanning in specimen A+B1, A+B2, A+B3 and A+B4 compared with a uniform sample processed with initial parameter A only.

The melt pools in regions with 20 layers of rescanning for A+B1, A+B2, A+B3, and A+B4 are shown in the first column of Figure 16 (a–e). Within the rescan regions, sub-grain cell size was measured both in melt pools resulting from the initial A parameters and in melt pools from  $B_n$  parameters, as presented in the second column of Figure 16 (f–j). After applying rescanning with the four selected parameters, all rescan regions showed a refined sub-grain cell size.

Parameters	Melt pool	Sub-grain cellular structure
A		

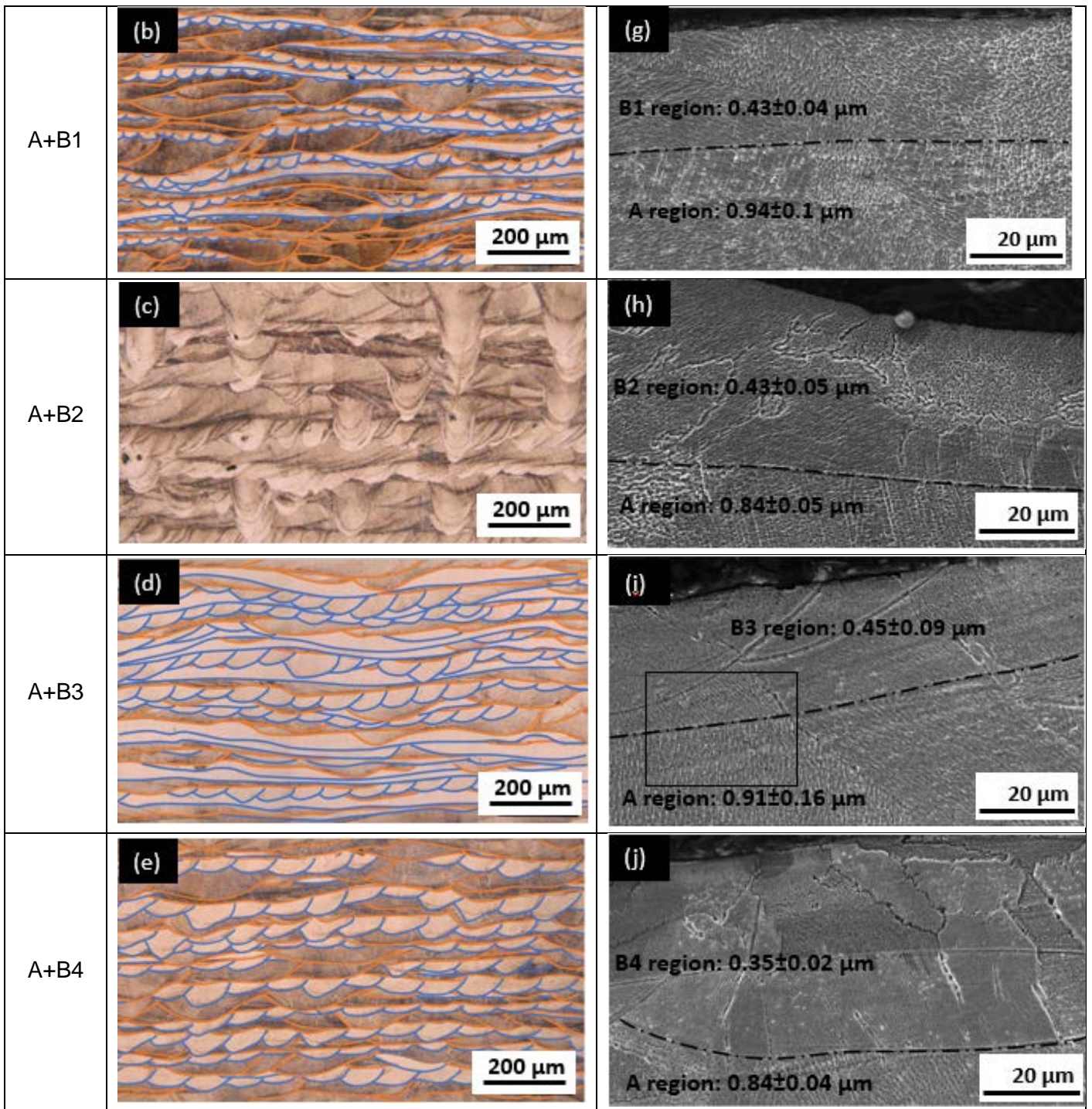


Figure 16 Melt pools in regions initially scanned with A (a–e) and rescanned with  $B_n$  parameters (b–e). Blue lines show rescanned melt pools and orange lines show initial scan melt pools. Corresponding sub-grain cellular structure (g–j), with black dashed line indicating the boundaries between initial and rescanned melt pools, and average cell sizes. Box inset in (i) is shown in Fig. 17.

The transition from finer to coarser sub-grain regions in specimen A+B3 is shown in Fig. 17 (a detail of the inset box region shown in Figure 16(i)). At the interface between the refined rescan melt tracks (blue) and coarser initial scan melt tracks (orange) there

is no apparent gradation in cell size, and the transition from coarse to finer across the melt track boundary appears to be sharp at this magnification. Therefore, the spatial distribution of cell size refinement is approximately equal to the size of the melt pools from rescanning (marked by blue lines in Fig. 16 (a–e)).

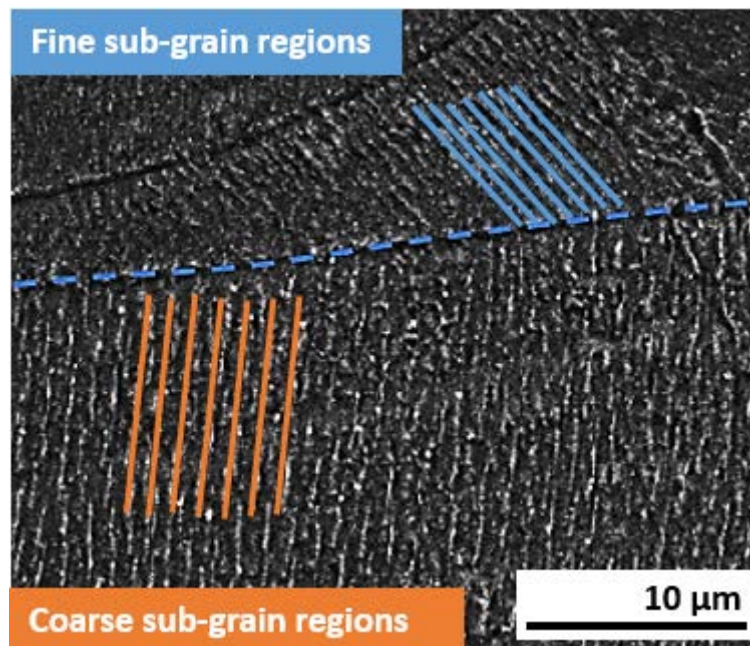


Figure 17 Transition from fine to coarse cell sizes at a melt pool boundary (dashed blue line) between initial scan parameters A (orange) and rescan parameters B3. Cellular structure spacings are highlighted with parallel lines in each region.

Figure 18 shows the measured cell size in both initial scanning regions (orange points) and rescan regions (blue points). Cell size measured from single scans with B1, B2, B3, B4 parameters are also marked (black points) as a comparison. The cell size in regions only scanned with initial parameter A was  $0.75\text{--}1.07\ \mu\text{m}$ , similar to the cell size measured in cube A1 ( $0.85\ \mu\text{m}$ , Fig. 12). Compared with cell size obtained in single scans, rescanning regions show a similar but slightly larger cell size, likely due to the slower cooling and added heat from adjacent scan tracks. Among the rescanning parameters, parameter B4, with the lowest linear energy density, resulted in the smallest refined cell size ( $0.35\ \mu\text{m}$ ), and the largest difference in cell size between initial scanning region ( $0.84\ \mu\text{m}$ ) and rescanning region ( $0.35\ \mu\text{m}$ ). The

Wilson-Rosenthal equation was also applied to predict the cell size in rescanning region and showed good agreement with experimental results. The nano-hardness of the A+B4 rescanned specimen in both initial scanning and rescanned regions was also measured. Rescanned hardness data were only taken from indents within rescanned melt pools, which were identified after indentation by microscopy. Compared with the region of initial scanning A, rescanning with B4 only showed a small, apparently insignificant increase in the average hardness values from  $2.87 \pm 0.11$  GPa to  $3.05 \pm 0.09$  GPa. Li et al. (2020) also reported a lack of correlation between cell size and hardening and argued that increasing dislocation density explains increases in hardness and strength of LPBF 316L SS, rather than cell size. An additional explanation for the insignificant effect on hardness may be the potential effects of rescanning on dynamic recrystallization and recovery, not only solidification (Sabzi et al., 2020). Thus, the potential for localised hardening and strengthening together with localised cell size refinement remains unclear and further work is needed to investigate dislocation density and these other potential effects of complex repeated heating cycles.

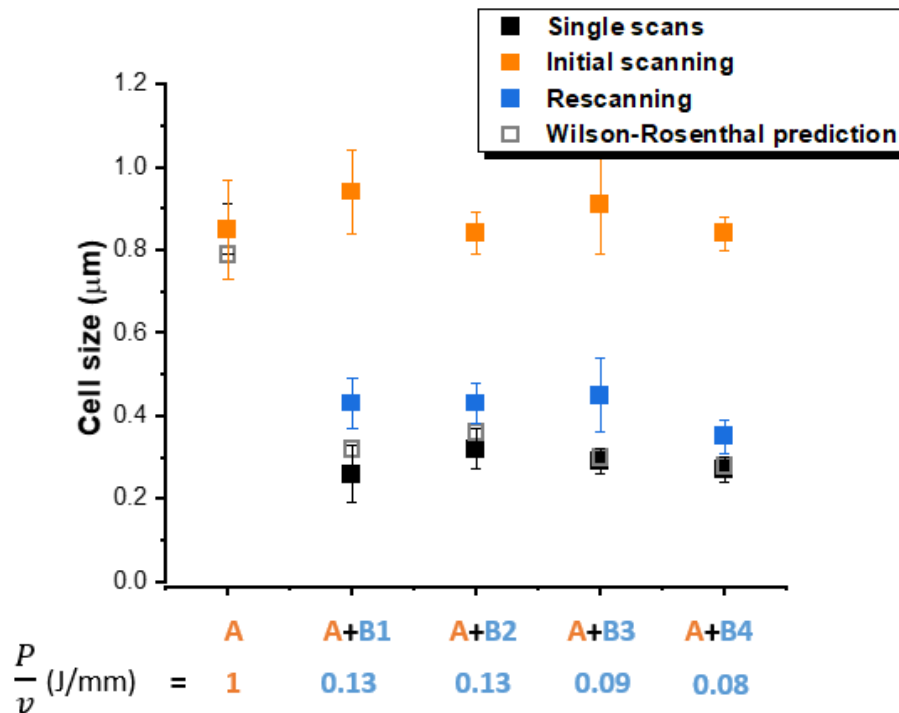


Figure 18 Measured and predicted cell sizes for both initial scanning and rescanning regions using parameter A+B1, A+B2, A+B3, A+B4.

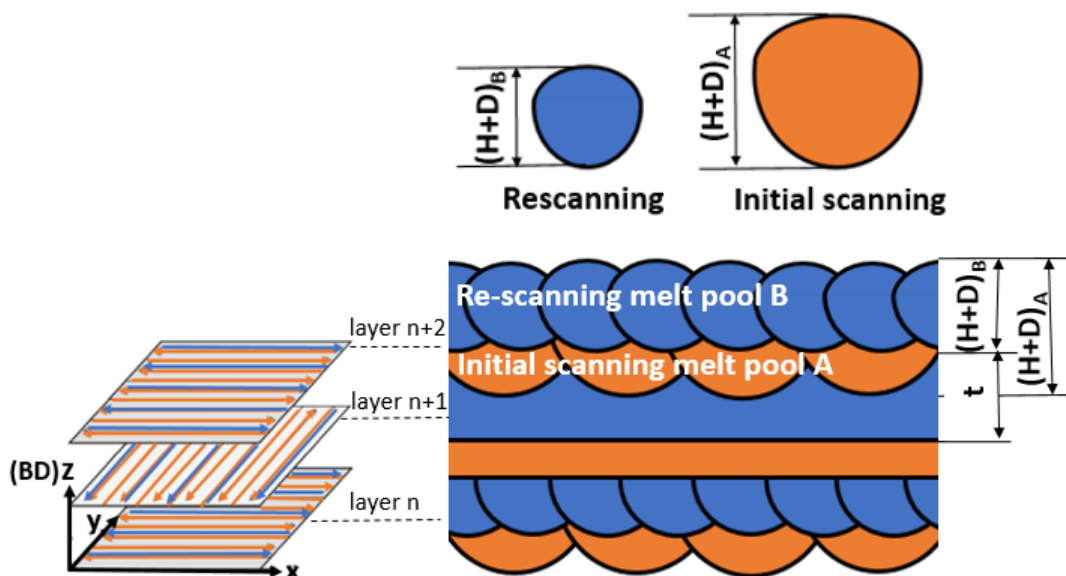


Figure 19 Schematic of rescanning strategy (left) and cross-sections of melt pools (right). Orange scans represent scanning with initial A parameter. Blue scans represent rescanning with B parameters.

Figure 19 shows a schematic of the rescanning strategy, with rescans following the same direction as initial scans in a given layer, and with scanning rotated by 90 degrees between each layer. The cross-sectional dimensions of the rescan melt pools (blue) relative to the initial melt pools (orange) and the total thickness of each layer ( $t$ ,

approximately equal to the powder layer thickness) plays an important role in the spatial distribution of microstructural heterogeneity caused by rescanning. Referring to these dimensions, there are three expected scenarios:

- (i) If the combined height and depth of melt pool B,  $(H+D)_B$ , is greater or equal to height and depth of melt pool A,  $(H+D)_A$  [i.e.,  $(H+D)_A - (H+D)_B \leq 0$ ], then  $t_A = 0$  and the microstructure will be dominated by that of the rescanned melt pool B.
- (ii) If  $0 < (H+D)_A - (H+D)_B < t$ , the rescanned region will contain both initial and rescanning modified microstructure. The thickness of the initial scan region will be  $t_A = (H+D)_A - (H+D)_B$  and the thickness of the rescanning modified microstructural region,  $t_B = t - t_A$ . Therefore, the microstructure of both the initial and rescanned tracks will be present.
- (iii) If  $(H+D)_A - (H+D)_B \geq t$ , then  $t_B = 0$  and the microstructure will be dominated by that of the initial melt pool A.

The dimensions of rescanned melt pools (B1, B2, B3, and B4) were measured and compared with initially scanned melt pools (A), as shown in Table 6. Based on the equations above,  $t_A$  and  $t_B$  were calculated and listed in Table 6. For all rescanned specimens, values of  $(H+D)_B$  are smaller than  $(H+D)_A$ , indicating that none of these microstructures are dominated by rescanned melt pools alone [i.e. no cases of scenario (i)]. In specimen A+B2,  $t_A$  is larger than the powder layer thickness ( $t = 30 \mu\text{m}$ ) and  $t_B = 0$ , as shown in Fig. 16 (c), and the rescanned tracks were covered by the next layers above [i.e. scenario (iii)]. All other rescanned specimens had values of  $t_A$  ranging from 0 to  $30 \mu\text{m}$ , indicating that both initial microstructure and modified microstructure exist in rescanning regions [i.e. scenario (ii)]. As shown in Fig. 16(b, d, and e), both orange and blue melt pools are visible. Among them, specimen A+B1



showed smallest proportion of blue rescanned melt pools in rescanning region with the smallest value of  $t_B$ .

Table 6 Measured depth + height (H+D) of initial and rescanned melt pool tracks in rescanned specimens.

	Specimen A+B1	Specimen A+B2	Specimen A+B3	Specimen A+B4
$(H+D)_A$ ( $\mu\text{m}$ )	$50.67 \pm 6.76$	$70.35 \pm 9.35$	$62.67 \pm 10.83$	$63.26 \pm 9.74$
$(H+D)_B$ ( $\mu\text{m}$ )	$22.07 \pm 2.62$	$16.47 \pm 2.91$	$44.43 \pm 4.98$	$45.80 \pm 3.35$
$t_A$ ( $\mu\text{m}$ )	28.6	53.88	18.24	17.46
$t_B$ ( $\mu\text{m}$ )	1.4	< 0	11.76	12.54

#### 4. Conclusion

Laser rescanning during LPBF additive manufacture with 316LSS was experimentally and analytically investigated in order to locally control the sub-grain cell size while maintaining high levels of densification with a commercially available 200 W single laser system. The main conclusions are:

1. Within a range of P-v processing space from  $50 \text{ W} < P < 200 \text{ W}$  and  $50 \text{ mm/s} < v < 1600 \text{ mm/s}$ , a range of sub-grain cell sizes from 0.26 to 0.85  $\mu\text{m}$  can be obtained in laser scan tracks that are likely suitable for processing multi-layer parts with high densification (continuous tracks with depth to width ratio  $DWR < 1$ ). With the same process parameters, sub-grain cell sizes measured from single laser scans were statistically similar to those in parts from multi-layer scans and rescanned regions. Therefore, single laser scan results can guide microstructural predictions for larger multi-layer parts.
2. Sub-grain cell size ( $d$ ) can be correlated to linear energy density ( $P/v$ ) according to an empirical power law relationship over a range of  $P/v$  values from 0.25 to 1 J/mm. Cell sizes measured from single laser scan experiments were

comparable to cell sizes in larger multi-scan and multi-layer parts. Wilson-Rosenthal equation predictions show that this can be explained by predicted increases in cooling rate with decreasing  $P/v$ , leading to refined cell sizes. However, predicted melt pool dimensions for single laser scans were unreliable.

3. Laser rescanning of each layer within a region of 20 layers increased the relative density by 0.21-0.42%. This increase was observed using laser rescanning parameters that caused process-induced defects when used as initial scan parameters. Therefore, LPBF parameters that are considered unsuitable for initial scanning and processing, may be suitable for heterogeneous microstructural control via rescanning.
4. In rescanned regions, the spatial distribution of the resulting heterogeneous microstructure is determined by the relative size of initial and rescanned melt pools and the powder layer thickness.
  - (i) When rescan melt pools are largest, the rescan microstructure will dominate.
  - (ii) When the rescan melt pools are smaller than the initial scans, but larger than the powder layer height, both initial and rescan microstructure will exist.
  - (iii) When the rescan melt pools are smaller than the initial scans and the powder layer height, the initial microstructure will dominate.
5. With a low-power laser (up to 200 W) and without rescanning, little variation in cell size (0.68–0.85  $\mu\text{m}$ ) was achieved while maintaining high densities (>99.55%). By implementing rescanning, a larger difference in cell size between the initial scanning region (0.84  $\mu\text{m}$ ) and the rescanning region (0.35  $\mu\text{m}$ ) can be achieved with a high level of density (99.96%) in a single LPBF process for

316L SS. The effect of cell size on hardness was negligible in this study, which may be due to the differences in dislocation density around refined sub-grain cells and the potential effects of dynamic recrystallization and recovery due to repeated heating cycles from scanning and rescanning.

### **Declaration of Competing Interest:**

The authors report no declarations of interest.

### **Acknowledgments:**

This work was supported by the faculty of Engineering and Physical Science at University of Southampton. The authors are also grateful for contributions of Dr. Dichu Xu (operation of Nanoindenter), Richard Dooler (operation of Concept Laser M2) and Geoff Howell (assistance with metallographic preparation).

## Reference:

- ADDITIVE, C., 2019a. 316L Powder for Additive Manufacturing.
- Additive, G., 2019b. GE Additive 316L Datasheet.
- ASTM, 2015. ASTM E2546-15 Standard Practice for Instrumented Indentation Testing.
- ASTM, 2017. Standard Test Methods for Density of Compacted or Sintered Powder Metallurgy (PM) Products Using Archimedes' Principle, p. 7.
- Casati, R., Lemke, J., Vedani, M., 2016. Microstructure and Fracture Behavior of 316L Austenitic Stainless Steel Produced by Selective Laser Melting. *Journal of Materials Science & Technology* 32, 738-744.
- Cherry, J.A., Davies, H.M., Mehmood, S., Lavery, N.P., Brown, S.G.R., Sienz, J., 2014. Investigation into the effect of process parameters on microstructural and physical properties of 316L stainless steel parts by selective laser melting. *The International Journal of Advanced Manufacturing Technology* 76, 869-879.
- Clymer, D.R., Cagan, J., Beuth, J., 2017. Power–Velocity Process Design Charts for Powder Bed Additive Manufacturing. *Journal of Mechanical Design* 139.
- Collins, P., Brice, D., Samimi, P., Ghamarian, I., Fraser, H., 2016. Microstructural control of additively manufactured metallic materials. *Annual Review of Materials Research* 46, 63-91.
- Di, W., Yongqiang, Y., Xubin, S., Yonghua, C., 2011. Study on energy input and its influences on single-track, multi-track, and multi-layer in SLM. *The International Journal of Advanced Manufacturing Technology* 58, 1189-1199.
- Eagar, T., Tsai, N., 1983. Temperature fields produced by traveling distributed heat sources. *Welding journal* 62, 346-355.
- Guo, Y., Jia, L., Kong, B., Wang, N., Zhang, H., 2018. Single track and single layer formation in selective laser melting of niobium solid solution alloy. *Chinese Journal of Aeronautics* 31, 860-866.
- Hao, L., Dadbakhsh, S., Seaman, O., Felstead, M., 2009. Selective laser melting of a stainless steel and hydroxyapatite composite for load-bearing implant development. *Journal of Materials Processing Technology* 209, 5793-5801.
- ISO, 2017. ISO 643:2017 Steels — Micrographic determination of the apparent grain size, p. 23.
- Katayama, S., Matsunawa, A., 1984. Solidification microstructure of laser welded stainless steels, *International Congress on Applications of Lasers & Electro-Optics*. Laser Institute of America, pp. 60-67.
- Keller, C., Mokhtari, M., Vieille, B., Briatta, H., Bernard, P., 2020. Influence of a rescanning strategy with different laser powers on the microstructure and mechanical properties of Hastelloy X elaborated by powder bed fusion. *Materials Science and Engineering: A*, 140474.
- King, W.E., Barth, H.D., Castillo, V.M., Gallegos, G.F., Gibbs, J.W., Hahn, D.E., Kamath, C., Rubenchik, A.M., 2014. Observation of keyhole-mode laser melting in laser powder-bed fusion additive manufacturing. *Journal of Materials Processing Technology* 214, 2915-2925.
- Kistler, N.A., Nassar, A.R., Reutzel, E.W., Corbin, D.J., Beese, A.M., 2017. Effect of directed energy deposition processing parameters on laser deposited Inconel® 718: Microstructure, fusion zone morphology, and hardness. *Journal of Laser Applications* 29, 022005.
- Li, Z., He, B., Guo, Q., 2020. Strengthening and hardening mechanisms of additively manufactured stainless steels: The role of cell sizes. *Scripta Materialia* 177, 17-21.

Matilainen, V., Piili, H., Salminen, A., Syvänen, T., Nyrhilä, O., 2014. Characterization of Process Efficiency Improvement in Laser Additive Manufacturing. *Physics Procedia* 56, 317-326.

Mills, K.C., 2002. Recommended values of thermophysical properties for selected commercial alloys. Woodhead Publishing.

Niendorf, T., Leuders, S., Riemer, A., Brenne, F., Tröster, T., Richard, H.A., Schwarze, D., 2014. Functionally Graded Alloys Obtained by Additive Manufacturing. *Advanced Engineering Materials* 16, 857-861.

Promoppatum, P., Yao, S.-C., Pistorius, P.C., Rollett, A.D., 2017. A comprehensive comparison of the analytical and numerical prediction of the thermal history and solidification microstructure of Inconel 718 products made by laser powder-bed fusion. *Engineering* 3, 685-694.

Rosenthal, D., 1941. Mathematical Theory of Heat Distribution during Welding and Cutting. *Welding Journal* 20, 220-234.

Rubenchik, A., Wu, S., Mitchell, S., Golosker, I., LeBlanc, M., Peterson, N., 2015. Direct measurements of temperature-dependent laser absorptivity of metal powders. *Applied optics* 54, 7230-7233.

Sabzi, H.E., Aboulkhair, N.T., Liang, X., Li, X.-H., Simonelli, M., Fu, H., Rivera-Díaz-del-Castillo, P.E., 2020. Grain refinement in laser powder bed fusion: The influence of dynamic recrystallization and recovery. *Materials & Design* 196, 109181.

Saunders, M., 2017. X marks the spot - find ideal process parameters for your metal AM parts.

Scipioni Bertoli, U., MacDonald, B.E., Schoenung, J.M., 2019. Stability of cellular microstructure in laser powder bed fusion of 316L stainless steel. *Materials Science and Engineering: A* 739, 109-117.

Tian, Y., Gora, W.S., Cabo, A.P., Parimi, L.L., Hand, D.P., Tammis-Williams, S., Prangnell, P.B., 2018. Material interactions in laser polishing powder bed additive manufactured Ti6Al4V components. *Additive Manufacturing* 20, 11-22.

Wang, X., Muñoz-Lerma, J.A., Sánchez-Mata, O., Attarian Shandiz, M., Brochu, M., 2018. Microstructure and mechanical properties of stainless steel 316L vertical struts manufactured by laser powder bed fusion process. *Materials Science and Engineering: A* 736, 27-40.

Xiao, Z., Chen, C., Hu, Z., Zhu, H., Zeng, X., 2020. Effect of rescanning cycles on the characteristics of selective laser melting of Ti6Al4V. *Optics & Laser Technology* 122, 105890.

Yasa, E., Kruth, J.-P., Deckers, J., 2011. Manufacturing by combining selective laser melting and selective laser erosion/laser re-melting. *CIRP annals* 60, 263-266.

Yasa, E., Kruth, J.P., 2011. Microstructural investigation of Selective Laser Melting 316L stainless steel parts exposed to laser re-melting. *Procedia Engineering* 19, 389-395.

Ye, J., Rubenchik, A.M., Crumb, M.F., Guss, G., Matthews, M.J., 2018. Laser absorption and scaling behavior in powder bed fusion additive manufacturing of metals, CLEO: Science and Innovations. *Optical Society of America*, p. JW2A. 117.

Yusuf, S., Chen, Y., Boardman, R., Yang, S., Gao, N., 2017. Investigation on Porosity and Microhardness of 316L Stainless Steel Fabricated by Selective Laser Melting. *Metals* 7.

Zhang, B., Li, Y., Bai, Q., 2017. Defect Formation Mechanisms in Selective Laser Melting: A Review. *Chinese Journal of Mechanical Engineering* 30, 515-527.